

A sinusoidal transformation of the visual field is the basis for periodic maps in area V2

Highlights

- The brain's maps of visual space are thought to preserve the topology of the retina
- Maps in tree shrew V2 contradict this expectation, exhibiting a periodic organization
- This mapping aligns with periodic patterns of V2 response properties and connections
- This suggests that cortical circuits are customized for specific regions of visual space

Authors

Madineh Sedigh-Sarvestani,
Kuo-Sheng Lee, Juliane Jaepel,
Rachel Satterfield, Nicole Shultz,
David Fitzpatrick

Correspondence

msarvestani@gmail.com

In brief

The brain contains multiple maps of visual space that are thought to preserve the 2D spatial relationships established in the retina. Sedigh-Sarvestani et al. discovered a new periodic map structure for visual space in V2 that violates this assumption and reveals an unexpected correspondence with periodic maps of stimulus features.

Article

A sinusoidal transformation of the visual field is the basis for periodic maps in area V2

Madineh Sedigh-Sarvestani,^{1,3,*} Kuo-Sheng Lee,² Juliane Jaepel,¹ Rachel Satterfield,¹ Nicole Shultz,¹ and David Fitzpatrick¹

¹Functional Architecture and Development of Cerebral Cortex, Max Planck Florida Institute for Neuroscience, Jupiter, FL 33458, USA

²Department of Basic Neurosciences, University of Geneva, Geneva 1211, Switzerland

³Lead contact

*Correspondence: msarvestani@gmail.com

<https://doi.org/10.1016/j.neuron.2021.09.053>

SUMMARY

Retinotopic maps of many visual areas are thought to follow the fundamental principles described for the primary visual cortex (V1), where nearby points on the retina map to nearby points on the surface of V1, and orthogonal axes of the retinal surface are represented along orthogonal axes of the cortical surface. Here we demonstrate a striking departure from this mapping in the secondary visual area (V2) of the tree shrew best described as a sinusoidal transformation of the visual field. This sinusoidal topography is ideal for achieving uniform coverage in an elongated area like V2, as predicted by mathematical models designed for wiring minimization, and provides a novel explanation for periodic banded patterns of intra-cortical connections and functional response properties in V2 of tree shrews as well as several other species. Our findings suggest that cortical circuits flexibly implement solutions to sensory surface representation, with dramatic consequences for large-scale cortical organization.

INTRODUCTION

The discovery of retinotopic maps, the orderly representations of the visual field in cortical and subcortical structures, has had an enormous impact on our understanding of the visual system and its development (Barlow, 1986; Kaas, 1997). Classic descriptions of retinotopic maps emphasize the spatial preservation of local and global retinal relationships as a transform in which (1) orthogonal axes of the visual field are mapped along orthogonal axes of the cortical surface and (2) progression across the map yields smooth and continuous unidirectional progression in the visual field with no reversals. Moreover, such an organization is predicted by computational models that achieve optimal coverage of visual space while minimizing wiring costs (Durbin and Mitchison, 1990; Goodhill and Willshaw, 1990; Yu et al., 2020). The primary visual cortex (V1) in a number of species adheres to these principles (Adams and Horton, 2003; Bosking et al., 2000; Chaplin et al., 2013; Garrett et al., 2014; Manger et al., 2002), and although deviations have been noted in higher visual areas (Angelucci et al., 2015; Roe and Ts'o, 1995; Tusa et al., 1979; Yu et al., 2020), no alternate framework has been proposed. Here we present evidence from studies of the secondary visual area (V2) of the tree shrew, a close relative of primates, for a dramatic departure from the classic framework of retinotopic maps.

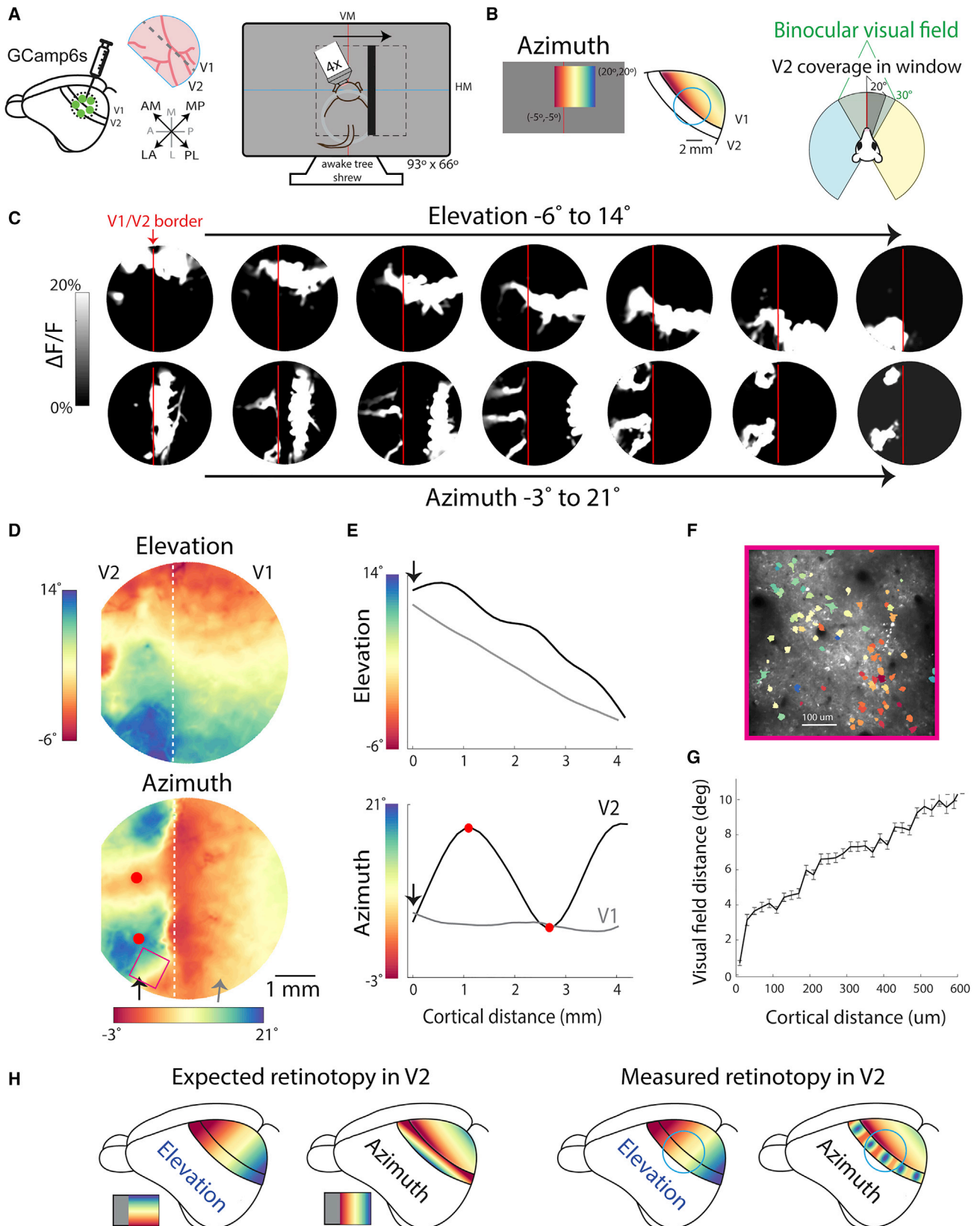
Using calcium imaging in awake animals, we found that the transformation of the visual field in V2 is sinusoidal, with representation of the two orthogonal axes of the visual field along the same elongated dimension of V2. Mathematical models

that simulate map formation show that the same principles that give rise to conformal maps in V1 give rise to sinusoidal maps in V2 and that the difference in mapping is due to different cortical area geometries. Moreover, we show, with anatomical tracing studies, that the organization of feedforward connections from V1 is sufficient to build the sinusoidal map in V2 from the conformal map in V1. Aside from its consequence on retinotopic maps, this intricate wiring also influences the organization of other functional feature maps, producing a banded pattern reminiscent of primate V2 (DeYoe and Van Essen, 1985; Hubel and Livingstone, 1987; Tootell et al., 1983).

Our study reveals a novel transform of the retinal surface on the cortex that arises from precise V1 connectivity to achieve optimal visual field coverage in V2 and is correlated with the large-scale organization of functional feature maps. This suggests that hierarchical connectivity between visual areas can give rise not only to increasing complexity in receptive field properties but also to increasing complexity in large-scale retinotopic organization. More importantly, our findings indicate that conformal or planar mapping of the sensory receptor surface is just one solution to optimal surface coverage and that cortical wiring can flexibly produce drastically different solutions under different conditions.

RESULTS

To characterize the retinotopic maps in layer 2/3 of V1 and V2, we used 1-photon wide-field and 2-photon single-cell



(legend on next page)

fluorescence microscopy to image neuronal calcium dynamics in awake, head-fixed, and restrained tree shrews trained to remain motionless during recordings. Retinotopic maps in adjacent regions of V1 and V2 were imaged simultaneously using a 3- to 5-mm cranial window implanted over the border of V1 and V2, covering the full ~ 1.5 -mm width of V2 along with a smaller fraction of V1 medial to the V1/V2 border (Figure 1A). The portions of V1 and V2 in the window typically covered a small region of the visual field between -10° – -20° azimuth and -15° – -15° elevation (Figure 1B). The medial and lateral border of V2 were defined based on the retinotopic map (STAR Methods). To quantify the retinotopic transform, we used stimuli that varied systematically in position along the elevation (vertical) or azimuth (horizontal) axes of visual space. To ensure that retinotopic maps were independent of eye movements, we simultaneously measured retinotopy maps and tracked pupil position (STAR Methods; Video S4) in the same animal. We found that awake tree shrews make small eye movements on the order of 2° – 5° during passive viewing and that these eye movements are unrelated to single-trial stimulus onset or offset. As a result, retinotopic maps were independent of the pattern of eye movements and consistent across sessions (Figures S1D and S1E).

Consistent with previous studies (Bosking et al., 2000; Kaas et al., 1972) of retinotopy in tree shrew V1, the elevation dimension of the contralateral visual field was mapped smoothly along the anteromedial-posterolateral (AM-PL) axis of V1, and the azimuth dimension was mapped smoothly along the orthogonal LA-MP axis (Figures 1C and 1D). For simplicity, we rotated the cranial window clockwise $\sim 45^{\circ}$ so that elevation and azimuth dimensions in V1 are vertical and horizontal, respectively.

The map of elevation in V2 appeared similar to that in V1, a relatively smooth progression with lower portions of the visual field represented by more anterior portions of cortex (Figures 1C and 1D). In contrast, the representation of azimuth was unlike any previously described retinotopic map. We had expected the azimuth map to be orthogonal to the elevation map so that a vertical (iso-azimuth) bar in visual space would give rise to a single band of activity in V2 parallel to the V1/V2 border that mirrored the activity in V1 (Figure 1H, left). Instead, a single vertical bar activated multiple distinct narrow bands in V2 that extended across its width (Figure 1C). The distance between the bands changed systematically as a function of the bar's position in visual space, merging for stimuli at the most central and paracentral represented locations.

The striking nature of this unusual mapping becomes evident in the pseudo-color map of azimuth (Figure 1D), which shows oscillations along the AM-PL axis of V2, with alternating regions sensitive to relatively more central or paracentral portions of the visual field. The oscillatory nature of this pattern is best appreciated by plotting the azimuth values corresponding to a linear trajectory in V2 (Figure 1D, arrowheads). Such a path on the cortex reveals a linear mapping of azimuth in V1 but a sinusoidal mapping in V2 (Figure 1E). The peaks and valleys of the oscillations lie at the center of the banded regions (red dots) in the azimuth map of V2 and correspond to “reversals” in the orderly progression in azimuth or the “merger” of two opposing gradients in mapping. The half-period of these oscillations, from the most central to most paracentral point, is 1.25 ± 0.35 mm (mean + SD across 6 animals; STAR Methods). Oscillating patterns for azimuth were found in every animal, albeit with variations in shape (Figure S1C).

Our wide-field results suggest that this large-scale oscillatory azimuth pattern occurs with smooth changes in visual field trajectory, but we thought it was important to confirm this with 2-photon cellular resolution. We focused on regions in V2 with the highest rate of change in azimuth, between central and relatively more paracentral bands (Figure 1D, box). Consistent with the wide-field results, single-cell measurements of visual field sensitivity (Figure 1F) showed smooth and continuous changes in azimuth location as a function of cortical distance between cell pairs (Figure 1G).

These results imply a fundamentally different transform for the mapping of retinotopy in V2 from what has been described in V1 and in most other visual areas (Figure 1H). A better understanding of this transform requires considering the fine-scale relationships between the maps of azimuth and elevation. We defined the spatial relationships between iso-elevation and iso-azimuth contours corresponding to equal distances in the visual field (Figure 2A). Consistent with previous studies, in V1, iso-azimuth and iso-elevation contours in the tree shrew (Bosking et al., 2000) and other animals (Adams and Horton, 2003; Chaplin et al., 2013; Garrett et al., 2014; Manger et al., 2002) exhibit a strong bias for orthogonality (Figures 2B and 2C). Just as elevation and azimuth contours are orthogonal in the visual field, they are orthogonal in V1 (Figure S2C); i.e., the transformation of the visual field in V1 is largely “conformal” in that it locally preserves angles in visual space (Schira et al., 2007; Schwartz, 1977). In contrast, the oscillating pattern of the map of azimuth in V2 is accompanied by a significant departure from this conformal

Figure 1. Tree shrew V2 exhibits a sinusoidal transform of the visual field

- (A) Calcium indicator injections in V1 and V2.
(B) Schematized azimuth map of V1. Right panel: Visual field represented by the portion of V2 in the imaging window.
(C) Magnitude of trial-averaged calcium response during equal intervals of bar position, thresholded at $\pm 20\%$ $\Delta F/F$. Red line, V1/V2 border.
(D) Azimuth and elevation maps. White dashed line, V1/V2 border. The box shows the two-photon field of view in (F). Red dots indicate reversal points in retinotopic gradients, also shown in (E).
(E) Extracted azimuth and elevation values corresponding to two straight lines in V1 and V2, indicated by gray (V1) and black (V2) arrowheads. Red dots indicate gradient reversals.
(F) Two-photon field of view (FOV) in V2, indicated in (D), and single-cell regions of interest (ROIs) colored by preferred azimuth.
(G) Pairwise distance in the visual field along azimuth versus cortical distance for cells in (F). Error bars indicate SEM.
(H) Unlike the expected orthogonal maps in V2, azimuth is also mapped along the long dimension, with nearby regions alternately representing more central or paracentral regions of the visual field. Anatomical data allow inference in regions outside of the window. Maps in polar coordinates are shown in Figures S5E and S5F.

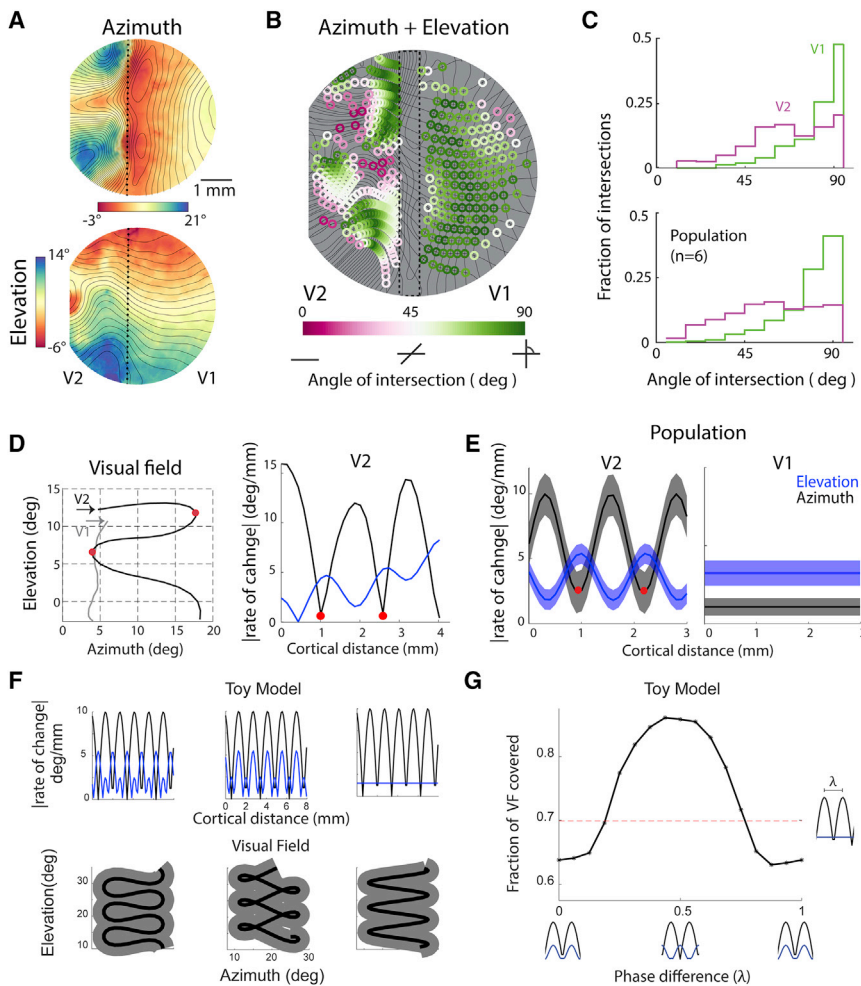


Figure 2. Azimuth and elevation gradients in V2 are not strictly orthogonal and oscillate out of phase

(A) Azimuth and elevation maps overlaid with 1° contour lines calculated from maps smoothed with a $500\text{-}\mu\text{m}$ nearest-neighbor filter (see Figure S2A for other filter sizes).

(B) Overlaid azimuth and elevation contours, with intersection angle in color.

(C) Distribution of intersection angles for V1 and V2 of the animals in (A) and (B) (top), pooled across additional animals (bottom). $p < 0.01$, two-sample Wilcoxon rank-sum test.

(D) Path in the visual field corresponding to the linear track in V2 in Figure 1D (left) and corresponding absolute value of the rate of change in the V2 path; red dots indicate gradient reversals in the V2 path; red dots indicate gradient reversals (right). Black and blue lines in the right panel represent azimuth and elevation, respectively.

(E) Population-average sinusoidal fits of the rate of change for paths in V2 and linear fits for paths in V1.

(F) Rates of change for azimuth and elevation with varying phase relationships, including sinusoids out of phase (left), sinusoids in phase (center), and sinusoidal azimuth but constant elevation (left), and corresponding paths in the visual field. The gray area represents an RF size of 5° , which approximates the measured RF size in V2 (Figure S3E). Data are produced from a simple mathematical model.

(G) Fraction of visual field covered versus azimuth-elevation phase offset for the simulated data in (F). The population-average phase offset (0.49) is near-optimal for maximum visual field coverage.

structure, with fewer intersections exhibiting an orthogonal angle (Figures 2B and 2C). Thus, the orderly topological representation of visual space that has been thought to be the hallmark of visual cortical areas is not preserved in V2.

Fully capturing the spatial relationship between maps of elevation and azimuth requires considering not only the angle of the contours but the rate of change of the contours across the cortical surface; i.e., the magnitude of the gradients (degree per millimeter) in azimuth and elevation and how they relate. To characterize the relative magnitude of the azimuth and elevation gradients, we consider a linear path in V1 and V2 (Figure 1D) and examine the corresponding trajectory in the visual field as well as its first derivative (Figure 2D, left and right, respectively). The visual field trajectory corresponding to the straight path in V1 is a line, indicating a linear transform, whereas the trajectory for V2 resembles a sinusoid (Video S1). As might be expected, the gradient magnitude for azimuth exhibits a strong oscillating pattern with low magnitude at the center of the central and paracentral bands where the gradient reverses (red dots) and high magnitude midway between the bands. This corresponds with higher amounts of V2 cortical space devoted to the most central and paracentral azimuths and relatively lower amounts devoted

to intermediate azimuths (Figure S2B). Interestingly, although the differences in gradient magnitudes for elevation are less, the elevation gradient magnitude also exhibits an oscillatory pattern that appears to be related to the azimuth gradients: the highest magnitude elevation gradients occur where the magnitude of the azimuth gradient is low (Figure 2D, right) and vice versa.

The inverse relationship of the azimuth and elevation gradient magnitudes is captured by fitting each gradient to a sine function (Figures S2D and S2E) and comparing the period and phase of each gradient. The population average ($n = 6$) period for azimuth and elevation gradients appears to be similar, 1.25 ± 0.35 mm for azimuth and 1.37 ± 0.36 for elevation. Two sinusoids with similar periods that are inversely correlated will be offset in phase by $1/2$ the period (λ). For the animal shown in Figure 2D, the phase offset in V2 is 0.46λ . To calculate the population average phase offset between azimuth and elevation gradients, we aligned all sinusoidal fits to azimuth gradients to a phase offset of 0 while maintaining relative phase offset between each animal's azimuth and elevation gradients. We then produced the sinusoidal plots in Figure 2E using the average sinusoidal fit parameters for all azimuth and elevation gradients. The population ($n = 6$) average of the phase offset in V2 is $0.49 \pm 0.23 \lambda$ (Figure 2E, left). In contrast,

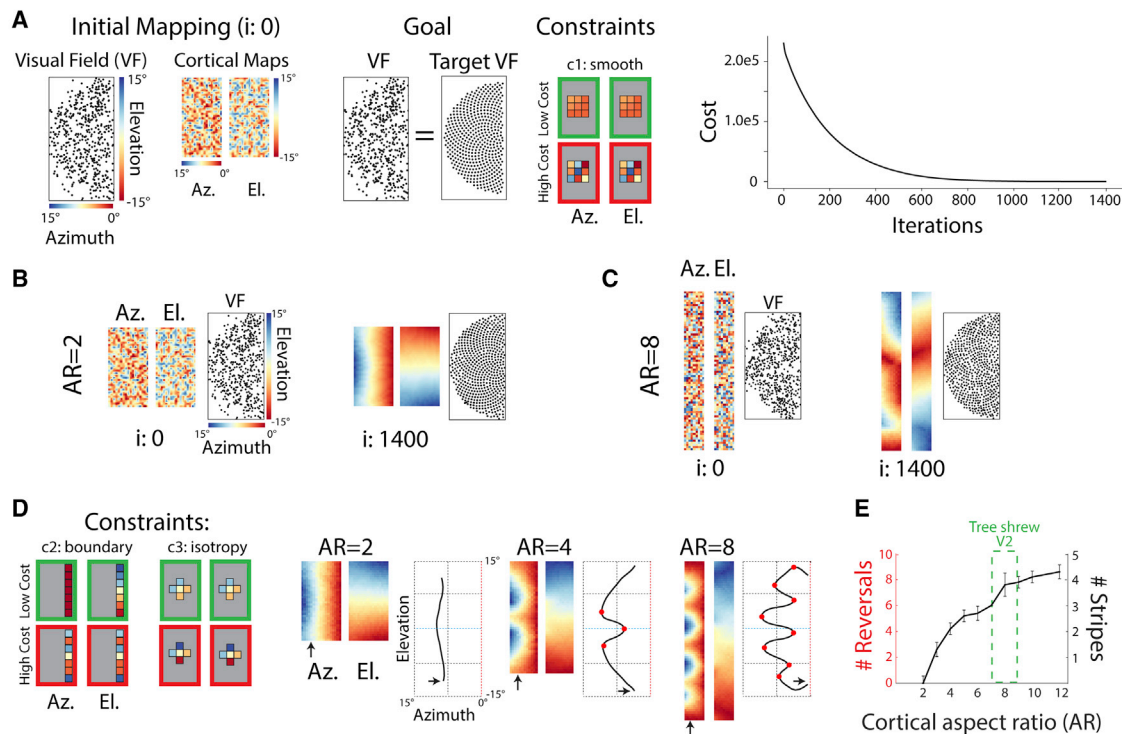


Figure 3. Sinusoidal retinotopy develops in elongated cortical areas

(A) Elastic net algorithm used to simulate the development of retinotopic maps from random initial conditions. The objective is to match RFs to an input set tiling the visual field (VF) while maintaining smooth nearest neighbor relations on the cortex (STAR Methods). The algorithm finds solutions that lower the total cost, eventually converging to a stable solution.

(B) At small aspect ratios (ARs), the final mapping consists of orthogonal maps of azimuth and elevation.

(C) At larger ARs, the final maps for azimuth and elevation are banded along the long axis of the cortex.

(D) Adding two constraints to the traditional elastic net produces maps similar to measured data (STAR Methods). Increasing the ARs produces increasingly banded azimuth maps but maintains smooth elevation maps. Traces correspond to the path in the visual field produced by a linear track in the cortex at the arrowhead. Red dots indicate azimuth reversals.

(E) Number of azimuth reversals and number of bands versus ARs. Error bars indicate SD from 10 simulations with different initial conditions. The green dashed box shows the range of ARs for the tree shrew V2 (Wong and Kaas, 2009).

V1 displays a linear gradient for azimuth and elevation (Figure 2E, right). In this figure, the average amplitude of the gradient for elevation is higher than that for azimuth in V1 simply because the path in V1 runs perpendicular to the elevation contours.

Why should there be such a complex pattern to the map of visual space in V2? One obvious possibility is that this sinusoidal structure is related to the markedly elongated shape of V2 in tree shrews as well as other species (Rosa and Krubitzer, 1999; Wolf et al., 1994; Table S1). Unlike the relatively isotropic V1, the tree shrew V2 is a narrow strip of the cortex that extends parallel to the border of V1 for 10–13 mm and orthogonal to the border for 1.5 mm, producing an aspect ratio of ~ 7 –9 (Wong and Kaas, 2009). We reasoned that the sinusoidal transform could serve to achieve coverage of the two dimensions of visual space in a cortical area that exhibits a pronounced spatial asymmetry, a solution that effectively uses the long cortical dimension to encode changes in azimuth and elevation (Video S2). Further support for this idea comes from modeling the oscillatory patterns and phase relationships of azimuth and elevation in V2. The similar periodicity and inverse correlation are ideal for optimizing coverage of the visual field (Figures 2F and 2G). Indeed,

the sinusoidal path we observe (Figure 2D) is reminiscent of the space-filling Peano curve in geometrical analysis and resembles the “boustrophedon” pattern that has been shown to achieve optimal spatial coverage with minimal path length in robotics path-planning literature (Choset and Pignon, 1998).

Thus, the retinotopic maps in both V1 and V2 appear to be organized in a fashion that optimizes coverage of the visual field, with differences in topology necessary to accommodate differences in the shape of the two areas. A strong test of this hypothesis is to ask whether the wiring minimization principles (Chklovskii and Koulakov, 2004) that have been shown to account for optimal coverage with a conformal transform in V1 drive optimal coverage with a sinusoidal transform in an area with the elongated shape of V2. To address this issue, we employed the well-established elastic net model (Goodhill and Willshaw, 1990; Yu et al., 2020). V2 is modeled as a sheet with point “neurons,” each with a receptive field (RF) in the visual field. Retinotopic maps are produced by color-coding V2 by the RF azimuth or elevation value of each neuron (Figure 3A, cortical maps). Initially, there is a random mapping between RFs in the visual field and neurons on the cortex (Figure 3A, left), although

different initial conditions produce qualitatively similar results (Figure S3A). The objective of the algorithm is to arrange the RFs so they match a set of input RFs that uniformly tile the visual field (target VF), with the wiring-length constraint of preserving map smoothness; e.g., nearby neurons on the cortex should have nearby RFs in the visual field. The algorithm iteratively optimizes the RFs to reduce the total cost associated with visual field coverage and smoothness until a stable state is reached (Figure 3A, right).

To understand the effect of cortical geometry on formation of maps (Wolf et al., 1994), we varied the elongation of the cortical sheet while maintaining the total cortical area, number of neurons, and all other parameters (STAR Methods). At small aspect ratios (ARs), the optimal final mappings are simple continuous representations of the visual field with orthogonal azimuth and elevation maps (Figure 3B). At larger ARs (Figure 3C), optimal visual field coverage is achieved by banded azimuth and elevation maps. This occurs because of the asymmetry in the number of neighbors along the two dimensions of the elongated cortex, which produces RF tiling with a 1D bias (Figure S3B) that manifests as striping of the cortical maps (Figure 3C). Although the elastic net applied to elongated cortical areas (Figure 3C) recapitulates the fundamental banded co-axial feature of retinotopic maps in V2 (Figure 1), its prediction differs from experimental data in significant ways. To improve the model, we added two additional biologically inspired constraints (Figure 3D): representation of the vertical meridian at the area's border (c2) and similarity in the local resolution along the two orthogonal axes of the cortical sheet (c3). The last constraint ensures that single RFs are not stretched significantly along horizontal or vertical axes (Figure S3E).

This full model could produce both types of maps observed in the relatively isotropic V1 and anisotropic V2. As the AR increased, the azimuth map became sinusoidal (Figure 3D, right), whereas the elevation map remained smooth because of the influence of the vertical meridian constraint. The oscillations that occurred in the azimuth map increased with increasing AR (Figures 3D and 3E), because of the local isotropy constraint, and were not dependent on the particular shape of the input RFs (Figure S3C). Maps formed oscillations even without the third constraint (Figure S3F), but they occurred at larger ARs, were fewer in number, and did not scale proportionally with increasing AR. Furthermore, elevation maps did not remain smooth for simulations with a rectangular target visual field. The third constraint acts locally (± 3 pixels) and does not restrict the cortical magnification factor to be isotropic along the short and long dimensions of V2.

Similar to our experimental observations (Figure 2D), the path in the visual field corresponding to a linear track along the model cortex (Figure 3D; Figure S3D) included several reversals (Figure 3D, red dots), which increased in number with increasing AR (Figure 3E, red). The model predicts that a cortical area with an AR similar to tree shrew V2 should have four sets of bands or four representations of the vertical meridian. The anatomical data from tree shrew callosal projections (Figures 5A and 5B) suggests five sets. The discrepancy may be due to several missing factors in our simplified model, including the constraint at the lateral border of V2 or the influence of the shape

of V1 on map development in V2. Nonetheless, our results confirm that the same biological principles can produce optimal coverage with conformal transforms along two dimensions in isotropic cortical areas such as V1 but produce a largely 1D sinusoidal transform in anisotropic areas such as V2. This is consistent with prior work on the influence of area shape and borders on retinotopic mapping (Wolf et al., 1994; Yu et al., 2020).

The functional data and model simulations provide evidence of a novel sinusoidal transformation of the retinal surface in V2 that is different from the traditional transform (Figure 4A). The most dramatic difference between the two representations can be seen in the map of azimuth (Figure 4A, right), with the single gradient map in V1 converting to a banded map in V2 with numerous gradient reversals at the most central and paracentral regions of the visual field. Because V2 receives dense projections from V1 (Lyon et al., 1998), we next examined whether the axonal connections from V1 to V2 are organized in a fashion that could support conversion from the map in V1 to that in V2. We began by examining the pattern of labeled axon terminals in V2 following injections of anterograde AAV viral tracers in V1 parallel to but displaced from the V1/V2 border, targeting neurons with RFs along an iso-azimuth axis of visual space but sparing neurons representing more central and paracentral regions. Consistent with prior observations (Sesma et al., 1984), we found discrete banded patterns of labeled terminals along the length of V2 (Figure 4B, left), as expected from the predictions of a sinusoidal transform (Figure 4B, right; Video S3). This experiment is analogous to activating V1 with a vertical bar in an iso-azimuth region of the visual field (Figure 1C).

Conversion from the 2D planar map in V1 to a co-axial sinusoidal map in V2 also predicts that injections displaced along the elevation axis of V1 and those displaced along the orthogonal azimuth axis should result in V2 axon terminal fields that are displaced along the same elongated dimension of V2 (Figure 4A). To test this prediction, we use differently colored viral tracers to create coarse color maps of elevation (Figure 4C, left) and azimuth (Figure 4C, right) along orthogonal dimensions of V1. We observe that, for both injection patterns, color variations in labeled terminals in V2 occur largely in the elongated dimension parallel to the V1/V2 border, consistent with our functional data (Figures 2B and 2C).

The pattern of labeled terminals in V2 following injections that vary in color along the azimuth axis of V1 is also consistent with smooth reversals in visual space evident in the functional map of V2 (Figures 1D and 4A). The axon terminals in V2 from the more central injection sites in V1 (yellow) are surrounded by the terminals derived from the more paracentral sites (green). Indeed, the spatial distribution of labeled terminals in V2 can be used to infer the location of central and paracentral gradient reversals in the map of visual space (Figure 4C, trace); reversals in the central visual field (rev_c) would be expected in the center of the bands of yellow terminals that are surrounded by green terminals, whereas reversals in paracentral regions (rev_p) would occur at the center of unlabeled regions surrounded by green terminals. The precision of this remapping to match the multiple reversals in V2 is also evident in patterns of labeled terminals from small neighboring injections of green and yellow tracers in V1 (Figure 4D). These injections are far from the central visual field

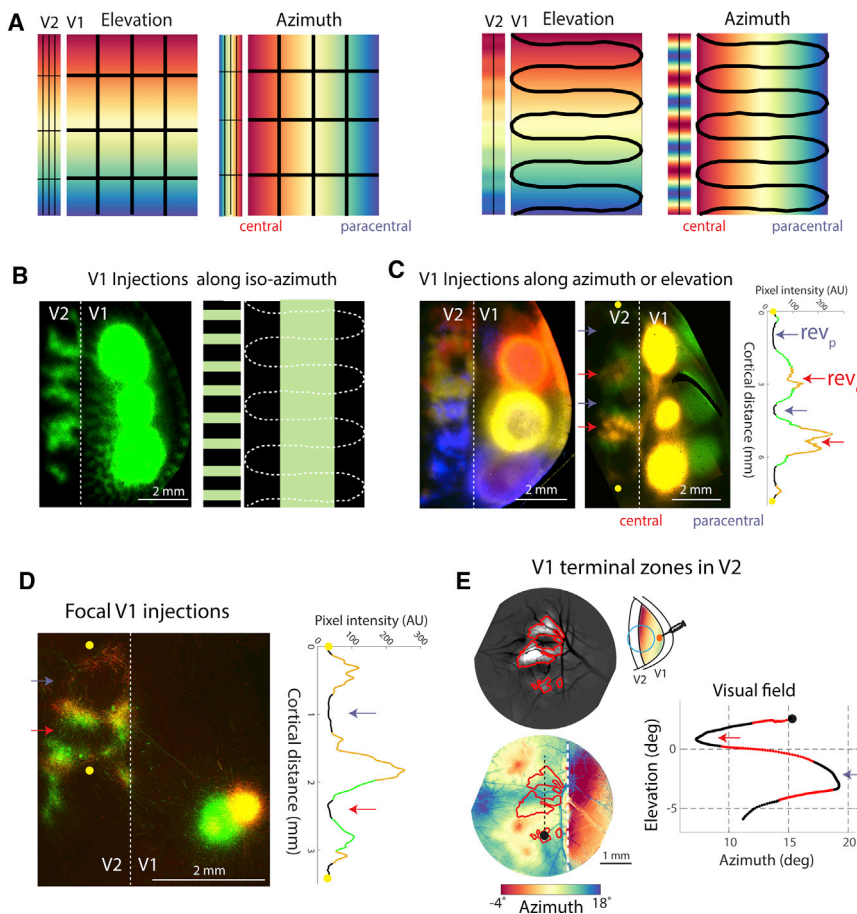


Figure 4. V1-V2 connectivity is sufficient to produce sinusoidal retinotopy in V2 from conformal retinotopy in V1

(A) Relationship between maps in V1 and V2 under a conformal or planar (left) and sinusoidal (right) transformation.

(B) Axon terminals in V2 produced from tdTomato AAV virus injections in V1 along an iso-azimuth axis in flattened section of left hemisphere (left) compared with the prediction from a sinusoidal transform of V1 (right). See also Figure S4A.

(C) Axon terminals in V2 produced from multi-colored AAV virus injections in V1 along the elevation-encoding axis (left) or azimuth-encoding axis (right). Trace of fluorophore color and intensity values for a line in V2 shows evidence of reversals in regions representing paracentral (rev_p) and central visual field (rev_c).

(D) Axon terminals in V2 produced by two focal AAV virus injections in V1 away from the V1/V2 border. Reversals are expected in unlabeled regions surrounded by the same-color terminals, as shown in the trace.

(E) Multiple axon patches in V2 produced by injection of the tdTomato AAV virus in V1 outside of the cranial window, imaged *in vivo* using a red filter (top) and azimuth map in same animal overlapped with axon projection contours (bottom). The trace shows the path in the visual field for the linear track in V2, with regions that pass through contours shown in red.

Scale bars in (C) and (D), 2 mm. STAR Methods show a detailed list of viruses. Additional injection experiments are shown in Figures S4A–S4C.

representation near the V1/V2 border and from the paracentral representation near the medial sinus. Each injection results in submillimeter thin bands of labeled terminals in V2 that surround terminal free regions, and the banded patterns change smoothly from green to yellow in between, reflecting the continuity of retinotopy at the two injection sites in V1.

What emerges from these experiments is a consistent pattern where sites in V1 that represent intermediate azimuth values give rise to labeled terminals in V2 surrounding label-free zones likely to represent central and paracentral reversals in azimuth (Figures 4C and 4D, traces). As a direct test of this hypothesis, we combined fluorescent tracer labeling produced by a single injection in V1 (Figures S4D and S4E) with functional retinotopic maps in the same animal (Figure 4E). Labeled terminals in V2 overlapped with regions of the azimuth map representing intermediate azimuth values. By comparing the distribution of labeled terminals with the corresponding map of visual space, it is apparent that the two prominent gaps in the distribution of labeled terminals correspond to reversals in azimuth, one central and the other paracentral (Figure 4E, trace). These results demonstrate that connections from V1 to V2 exhibit the fine-scale topography sufficient to build the sinusoidal co-axial transform in V2 from the conformal orthogonal transform in V1.

We further tested the consistency between anatomical projections and retinotopic maps by injecting a viral tracer in V1 of the

opposite hemisphere and studying the pattern of inter-hemispheric callosal terminals in V1 and V2 (Figures 5A–5D). Callosal projections are known to terminate in regions representing the vertical meridian (Cusick et al., 1985; Cusick and Lund, 1981; Houzel et al., 2002; Hubel and Wiesel, 1967; Innocenti et al., 2002; Cusick et al., 1984). We therefore expected to see a banded pattern of callosal terminal zones in V2 (Figure 5A) because the azimuth map of V2 has multiple periodic representations of the vertical meridian. As expected, injections in V1 restricted to the central $\sim 5^\circ$ of the retinotopic map produced a banded periodic pattern in V2 of the same hemisphere as well as V2 of the opposite hemisphere (Figure 5B, yellow). Injections in regions of V1 representing the paracentral visual field produced callosal projections only at the border between V1 and V2 (Figure 5B, green), consistent with the known highly compressed ipsilateral field representation in this region (Bosking et al., 2000). To further confirm the relationship between the periodic nature of the functional retinotopy maps and the periodic pattern of anatomical callosal projections in V2, we imaged callosal terminal zones in an animal with an existing cranial window (Figure 5C). We found that callosal terminal zones are biased toward the vertical meridian and surrounding $\sim 5^\circ$ (Figure 5D). Our results explain previous puzzling observations of a prominent banded pattern of callosal projections in the tree shrew V2 (Cusick et al., 1985). A similar

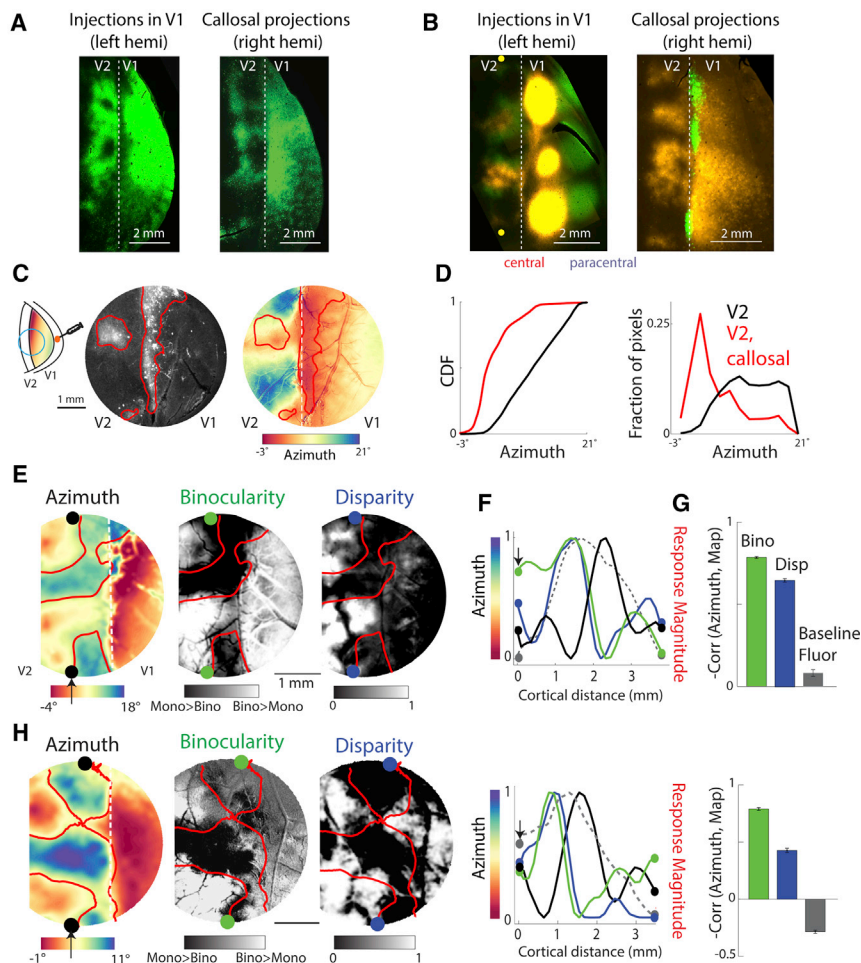


Figure 5. Functional feature maps in V2 are correlated with anatomical projection and retinotopy maps

(A) Flattened sections showing ipsilateral (left) and contralateral (right) axon projections in V2 produced by injections in V1.

(B) Same as (A), but 6 injections were made in the left V1, each set of 3 along an iso-azimuth axis in V1. Callosal projections from paracentral V1 (green) are limited to the V1/V2 border, whereas callosal projections from central V1 (yellow) form bands in V2. Green terminals in right hemisphere correspond to known compressed ipsilateral representation at the V1/V2 border (Bosking et al., 2000).

(C) Callosal projections within the imaging window produced by virus injections in V1 along an iso-azimuth axis in the contralateral V1 (Figure 4B), thresholded at 50% to produce contours, and azimuth map in the same animal overlapped with contours (right).

(D) Cumulative distribution function (CDF) (left) and histogram (right) of azimuth values for all pixels in V2 versus the pixels within the callosal terminal zone contours (red) show a central visual field bias for V2 pixels in callosal recipient regions.

(E) Functional maps in the same animal. Shown are the azimuth map overlaid with contour lines indicating the mid-point of the azimuth range, and a map of relative binocularity (Bino) and relative horizontal disparity sensitivity (Disp) (STAR Methods). All feature maps are thresholded ± 1 SD of the mean and normalized.

(F) Extracted pixel values for the azimuth and normalized feature maps corresponding to a line in V2, indicated by the arrowhead in (E).

(G) Mean pixel-wise correlations between the azimuth and feature maps in V2; Bino, -0.78 ± 0.01 ; Disp = -0.71 ± 0.01 ; GCaMP, -0.08 ± 0.02 . Negated correlation values are shown for easier interpretability. Error bars indicate SEM of 1,000 bootstraps.

(H) Same as (E) for a different animal. Bino, -0.79 ± 0.01 ; Disp, -0.44 ± 0.02 ; GCaMP, 0.28 ± 0.01 . See also Figure S5D.

observation of non-uniform retinotopy with periodically interleaved “islands” representing relatively more central and peripheral regions of the visual field has been reported in ferrets (Manger et al., 2002). Similar to our findings, acallosal regions of the retinotopy map in the secondary visual cortex of ferrets represented relatively more peripheral regions of the visual field (Manger et al., 2002).

Does sinusoidal retinotopy have significance for understanding the spatial distribution of functional properties in V2? In V1, neurons near the representation of the vertical meridian are more sensitive to binocular stimuli (Berman et al., 1982). Given the multiple periodic representations of the vertical meridian in V2, we wondered whether this would be accompanied by a periodic pattern in the processing of binocular information, with central regions exhibiting greater sensitivity to binocularly viewed stimuli. The region of V2 from which we record in our cranial window represents a relatively small region of the visual field (approximately -10° to 20°). This is well within the binocular visual field of the tree shrew (Figure 1B), which extends up to

30° on each visual hemifield for a total of 60° (Kaas et al., 1972). However, within this binocular region, there may exist subregions with a relatively stronger responses to binocular stimuli.

To determine whether V2 exhibits a map of relative binocularity, we measured the response to retinotopy stimuli viewed binocularly, or monocularly through the contralateral eye, and subtracted them to highlight relative differences in binocularity (STAR Methods; Kaskan et al., 2009)). We found interleaved regions of V2 that were relatively more binocular with greater responses for binocularly presented stimuli relative to the monocular presentation or more monocular with greater responses for monocularly presented stimuli. Notably, the overall pattern of binocular- or monocular-preferring regions was highly correlated to the azimuth map in the same animal (Figures 5E–5G). As predicted, V2 regions that represented more central regions of the visual field were more binocular compared with regions that represented paracentral regions. Our findings show that the sinusoidal retinotopy is correlated with a differential distribution of

binocular sensitivity that reflects a retinotopic bias within the binocular region of the visual field.

The integration of binocular information allows, but does not ensure, the estimation of depth from horizontal retinal disparity. We thus wondered whether differences in binocularity between relatively central and paracentral regions of V2 would be accompanied by differentially represented binocular disparity sensitivity across V2 retinotopic map. Using two-photon single-cell imaging, we confirmed that neurons in V2 are disparity tuned (Figures S5A and S5B). For wide-field imaging, we were interested in measuring the relative disparity sensitivity across the bands of V2. We therefore measured the pooled response to red/green random-dot stereograms drifting in various directions with and without horizontal disparity cues and subtracted the two resulting maps (STAR Methods). As might be expected, bands of V2 that represent more central regions of visual space exhibited higher sensitivity to horizontal disparity than those representing paracentral regions. (Figure 5E).

We found that the periodic azimuth map in V2 was correlated with periodic changes in sensitivity to different functional features. We extracted the pixel values along a line in V2 running across the bands at the same location in all maps (Figure 5F). The co-localized maxima and minima of the normalized curves corresponding to feature maps (colored lines) indicate their similarity along a line in V2. We calculated the pixel-wise correlation between the azimuth map and feature maps (Figure 5G) and found the strongest correlation between the azimuth and binocularity map (0.79 ± 0.01 SEM of 1,000 bootstraps). Furthermore, we found small or oppositely signed correlations between the pattern of GCaMP expression and the azimuth map (-0.28 ± 0.01 ; Figure S5C), ruling out the possibility that these correlations are simply due to a shared and non-uniform fluorophore expression pattern. Data for a second animal are shown in Figure 5H. We found that the sinusoidal transform we discovered in V2 not only has functional significance for retinotopic sensitivity but also correlates with periodic variations in sensitivity to binocular stimuli across cortical space. We show that complex retinotopy coupled with differences in feature sensitivity across the retinotopic map can produce so-called functional specializations, regions of the cortex with functionally distinct clusters of neurons likely to reflect behaviorally relevant processing of information from different regions of the visual space.

DISCUSSION

From the earliest descriptions of retinotopic maps in the brain, accumulated evidence has supported a fundamental principle for retinotopic organization, best described as a conformal transform that preserves the two dimensions of the visual field, and their orthogonal relationship, globally and locally. A specific formulation of the conformal transform (Schwartz, 1977) successfully predicts retinotopic maps in primate V1, and similar transforms that preserve the two-dimensional planar layout of the retina are thought to underlie retinotopic organization across visual areas and species. Our results challenge the universality of this perspective, demonstrating a novel sinusoidal (i.e., periodic) retinotopic mapping that does not preserve the planar structure of the retina globally. However, this mapping exhibits the fine-

scale properties ascribed to traditional maps—smooth coverage of visual space and adherence to wiring minimization—and is optimal for achieving this within the elongated spatial constraints of V2. This unique retinotopic transform and the correlated connectivity and functional specializations it embodies suggest a novel framework for conceptualizing similar periodic banded patterns described in squirrels (Kaas et al., 1989), ferrets (Manger et al., 2002), cats (Boyd and Matsubara, 1994; Sanides and Albus, 1980), and possibly primates (Abel et al., 2000; Olavarria and Abel, 1996; Roe and Ts'o, 1995; Rosa et al., 1988; Rosa, 1997; Shipp and Zeki, 2002).

It is important to emphasize that the map structure we identified is not just a regional distortion within an overall conformal map structure like the fine-scale discontinuities in the mapping of visual space that have been suggested to accommodate ocular dominance columns in V1 (Blasdel and Campbell, 2001; Najafian et al., 2019). Instead, our results illustrate a global non-conformal structure for retinotopic mapping where the conventional orthogonal relationship of azimuth and elevation is replaced with a broad range of intersection angles that allow azimuth and elevation to co-vary along the same axis in cortical space. Thus, retinotopic transforms are more diverse than we have appreciated, and we have much to learn about the mechanisms that shape the topological structure of neural representations (Benson et al., 2012; Rosa, 2002).

The functional measurements of periodic retinotopic maps in V2 are further supported by periodic patterns of V2 connectivity—inputs from V1 of the same hemisphere and from the opposite hemisphere through the *corpus callosum*. Callosal projections are known to terminate near representation of the vertical meridian (Cusick et al., 1985; Cusick and Lund, 1981; Houzel et al., 2002; Hubel and Wiesel, 1967; Innocenti et al., 2002; Cusick et al., 1984); thus, periodic callosal projections are consistent with interdigitated regions representing central (vertical meridian) and paracentral regions of the visual field. Notably, the correspondence between the periodic pattern of callosal projections and retinotopic maps in the secondary visual cortex is not unique to tree shrews but has also been reported in ferrets (Manger et al., 2002). We found that callosal recipient regions in V2, representing the central visual field, also had increased binocular sensitivity. This increased binocular sensitivity could be mediated by selective targeting of callosal projections to central regions. However, the contribution of callosal inputs to neuronal binocularity cannot be assumed because it appears to vary for cortical areas and species (Dehmel and Löwel, 2014; Diao et al., 1983; Minciacchi and Antonini, 1984). Interestingly, callosal inputs appear to be causally related to binocularity in species, such as tree shrews, that lack ocular dominance columns in V1 (Andelin et al., 2020).

Although studies in other species did not have access to all of the converging lines of functional and anatomical evidence presented here, the following similarities suggest that some form of periodic visual field representation may exist in V2 of other species. Puzzling reversals in the orderly progression of the map of visual space have been noted in V2 of the macaque, with specific mention that they were present in regions that were rich in disparity-sensitive neurons (so-called thick cytochrome oxidase stripes; Roe and Ts'o, 1995). This is similar to our findings of increased sensitivity to disparity stimuli for central regions of

the retinotopy map in V2, which also contain reversals. Close inspection of RF positions measured along the long axis of V2 in the *Cebus* monkey (Rosa et al., 1988), macaque (Roe and Ts'o, 1995; Shipp and Zeki, 2002), and marmoset (Rosa et al., 1997) reveals small and continuous retinotopic oscillations reminiscent of the pattern described here. Similar observations were noted in cat areas 18 and 19 (Tusa et al., 1979). There is no evidence yet that the pattern of connections from V1 to V2 in these species is organized in a fashion that would support these oscillations. However, banded callosal connections within V2 that selectively target the cortical representation near the vertical meridian (Manger et al., 2002; Sanides and Albus, 1980) have been noted in several species (Boyd and Matsubara, 1994; Innocenti et al., 2002; Manger et al., 2002; Olavarria and Abel, 1996; Rosa and Manger, 2005). Our findings set up a hypothesis for a common organization of V2 that can be tested with optical imaging in marmosets and other smooth-brained primates.

Our results challenge another principle of retinotopic mapping: the idea that reversals in progression in visual space define the boundaries of cortical areas (Garrett et al., 2014; Sereno et al., 1994). We consider V2 of the tree shrew a single area, despite having multiple reversals, based on previously established cytoarchitecture findings (Wong and Kaas, 2009) and our observation that each region between the azimuth reversals maps a range of azimuths for a limited extent of elevation. Our simulations show multiple reversals form within the retinotopic map of a single area given a sinusoidal transform. Our results as well as recent findings in the primate extrastriate cortex (Yu et al., 2020) suggest a more nuanced approach to the one-to-one use of reversals in area delineation as exercised in studies of the mouse visual cortex (Garrett et al., 2014; Juavinett et al., 2017; Wang and Burkhalter, 2007). To some degree, the definition of a “functional visual area” is a matter of semantics based on assumptions of the underlying retinotopic transform. Nomenclature aside, the common theme to these functional parcellations is the correlation between retinotopic location, functional properties, and connectivity that suggests specialized contributions to visual function.

Why does V2 exhibit this unusual retinotopic transform? The log-polar conformal transform underlying retinotopy maps in primate V1 produces some invariance to image rotations and dilations (Schwartz, 1983), which may reflect an optimization to the structure of visual input. It is not clear that sinusoidal mapping also produces invariance to particular image transformations, but further work, including more rigorous quantification, may clarify this issue. However, our simulations do suggest that sinusoidal retinotopy reflects an optimization to geometric constraints imposed by the shape of V2.

We show that a periodic transform achieves optimal coverage and continuity in RF locations of neighboring neurons within elongated cortical areas such as V2. By this description, the significance of the sinusoidal organization lies in preserving the local properties of a planar conformal representation within a unique nonplanar global organization. But why is V2 elongated in so many species (Rosa and Krubitzer, 1999) in the first place? One possibility is that the shape of V2 is constrained during development by the earlier maturation of vertical meridian representation in nearby areas, including V1 (Mundinano et al., 2015;

Rosa, 2002). Another possibility is that V2 has an elongated shape because the sinusoidal organization facilitates neural circuit interactions challenging to achieve in a conformal setting where central and paracentral regions of visual space are distributed over a wider region of the cortex. One such computation may be integration of context surrounding the center of gaze, useful for discrimination of object boundaries and planning saccadic eye movements.

Yet another interesting possibility is that this organization regionalizes circuits specialized for extracting different types of information from different locations in visual space, a refinement of the parallel streams hypothesis that includes retinotopy as one of the functional variants (Brown et al., 2005; Mishkin and Ungerleider, 1982; Schneider, 1969). In fact, reports of a visual field bias across the dorsal and ventral streams (Sheth and Young, 2016; Yu et al., 2015) and recent observations of functional specializations correlated with visual field sensitivity in human ventral visual areas support this idea (Hasson et al., 2002; Kamps et al., 2020). We predict that analysis of the functional properties that exhibit clustering in other animals, such as cats and primates, will reveal additional visual field specializations that support niche-adaptive visual behaviors. Our work highlights a powerful role of retinotopy in anchoring the anatomical and functional organization of cortical circuits within the visual hierarchy (Arcaro and Livingstone, 2017).

STAR★METHODS

Detailed methods are provided in the online version of this paper and include the following:

- KEY RESOURCES TABLE
- RESOURCE AVAILABILITY
 - Lead contact
 - Materials availability
 - Data and code availability
- EXPERIMENTAL MODEL AND SUBJECT DETAILS
- METHOD DETAILS
 - Behavioral acclimation
 - Craniotomy and intra-cortical expression of viral vectors
 - Chronic recording setup and head fixation
 - Eye tracking
 - Calcium imaging experiments
 - Two-photon imaging experiments
 - Visual stimulus methods
 - Tracer injections
 - Fixation and immunostaining
 - Alignment of functional maps with anatomical data from the same animal
 - Data Analysis
 - Model methods
- QUANTIFICATION AND STATISTICAL ANALYSIS

SUPPLEMENTAL INFORMATION

Supplemental information can be found online at <https://doi.org/10.1016/j.neuron.2021.09.053>.

ACKNOWLEDGMENTS

We thank Susan Freling, Molly Geisler, Dr. Idris El-Amin, Solana Liu, Jessica Kerr, and the Animal Resource Center at the Max Planck Florida Institute for Neuroscience (MPFI). We also thank members of the Fitzpatrick lab as well as Seneca Harberger and Matthew Krause for discussions. This work was supported by R01 EY006821 (to D.F.), F32 EY026463 (to M.S.-S.), and the MPFI.

AUTHOR CONTRIBUTIONS

M.S.-S. designed the study and collected and analyzed the data. K.-S.L. contributed to study design. K.-S.L. and J.J. contributed to data collection. R.S. and N.S. performed histological processing and imaging. M.S.-S. and D.F. wrote the manuscript. D.F. contributed to study design and provided financial support.

DECLARATION OF INTERESTS

The authors declare no competing interests.

Received: January 29, 2021

Revised: July 21, 2021

Accepted: September 23, 2021

Published: October 22, 2021

SUPPORTING CITATIONS

The following references appear in the supplemental information: Felleman and Van Essen (1991); Majka et al. (2016); Sereno et al. (2015); Sincich et al. (2003).

REFERENCES

- Abel, P.L., O'Brien, B.J., and Olavarria, J.F. (2000). Organization of callosal linkages in visual area V2 of macaque monkey. *J. Comp. Neurol.* **428**, 278–293.
- Adams, D.L., and Horton, J.C. (2003). A precise retinotopic map of primate striate cortex generated from the representation of angioscotomas. *J. Neurosci.* **23**, 3771–3789.
- Andelin, A.K., Doyle, Z., Laing, R.J., Turecek, J., Lin, B., and Olavarria, J.F. (2020). Influence of ocular dominance columns and patchy callosal connections on binocularity in lateral striate cortex: Long Evans versus albino rats. *J. Comp. Neurol.* **528**, 650–663.
- Angelucci, A., Roe, A.W., and Sereno, M.I. (2015). Controversial issues in visual cortex mapping: Extrastriate cortex between areas V2 and MT in human and nonhuman primates. *Vis. Neurosci.* **32**, E025.
- Arcaro, M.J., and Livingstone, M.S. (2017). A hierarchical, retinotopic proto-organization of the primate visual system at birth. *eLife* **6**, 1–24.
- Barlow, H.B. (1986). Why have multiple cortical areas? *Vision Res.* **26**, 81–90.
- Benson, N.C., Butt, O.H., Datta, R., Radoeva, P.D., Brainard, D.H., and Aguirre, G.K. (2012). The retinotopic organization of striate cortex is well predicted by surface topology. *Curr. Biol.* **22**, 2081–2085.
- Berman, N., Payne, B.R., Labar, D.R., and Murphy, E.H. (1982). Functional organization of neurons in cat striate cortex: variations in ocular dominance and receptive-field type with cortical laminae and location in visual field. *J. Neurophysiol.* **48**, 1362–1377.
- Blasdel, G., and Campbell, D. (2001). Functional retinotopy of monkey visual cortex. *J. Neurosci.* **21**, 8286–8301.
- Bobier, W.R., Campbell, M.C.W., and Hinch, M. (1992). The influence of chromatic aberration on the static accommodative response. *Vision Res.* **32**, 823–832.
- Bosking, W.H., Kretz, R., Pucak, M.L., and Fitzpatrick, D. (2000). Functional specificity of callosal connections in tree shrew striate cortex. *J. Neurosci.* **20**, 2346–2359.
- Boyd, J., and Matsubara, J. (1994). Tangential organization of callosal connectivity in the cat's visual cortex. *J. Comp. Neurol.* **347**, 197–210.
- Brown, L.E., Halpert, B.A., and Goodale, M.A. (2005). Peripheral vision for perception and action. *Exp. Brain Res.* **165**, 97–106.
- Chaplin, T.A., Yu, H.-H., and Rosa, M.G.P. (2013). Representation of the visual field in the primary visual area of the marmoset monkey: magnification factors, point-image size, and proportionality to retinal ganglion cell density. *J. Comp. Neurol.* **521**, 1001–1019.
- Chen, T.W., Wardill, T.J., Sun, Y., Pulver, S.R., Renninger, S.L., Baohan, A., Schreier, E.R., Kerr, R.A., Orger, M.B., Jayaraman, V., et al. (2013). Ultrasensitive fluorescent proteins for imaging neuronal activity. *Nature* **499**, 295–300.
- Chklovskii, D.B., and Koulakov, A.A. (2004). Maps in the brain: what can we learn from them? *Annu. Rev. Neurosci.* **27**, 369–392.
- Choset, H., and Pignon, P. (1998). Coverage Path Planning: The Boustrophedon Cellular Decomposition. In *Field and Service Robotics*, A. Zelinsky, ed. (Springer), pp. 203–209.
- Cusick, C.G., and Lund, R.D. (1981). The distribution of the callosal projection to the occipital visual cortex in rats and mice. *Brain Res.* **214**, 239–259.
- Cusick, C.G., Gould, H.J., 3rd, and Kaas, J.H. (1984). Interhemispheric connections of visual cortex of owl monkeys (*Aotus trivirgatus*), marmosets (*Callithrix jacchus*), and galagos (*Galago crassicaudatus*). *J. Comp. Neurol.* **230**, 311–336.
- Cusick, C.G., MacAvoy, M.G., and Kaas, J.H. (1985). Interhemispheric connections of cortical sensory areas in tree shrews. *J. Comp. Neurol.* **235**, 111–128.
- Dehmel, S., and Löwel, S. (2014). Cortico-cortical interactions influence binocularity of the primary visual cortex of adult mice. *PLoS ONE* **9**, e105745.
- DeYoe, E.A., and Van Essen, D.C. (1985). Segregation of efferent connections and receptive field properties in visual area V2 of the macaque. *Nature* **317**, 58–61.
- Diao, Y.-C., Wang, Y.-K., and Pu, M.-L. (1983). Binocular responses of cortical cells and the callosal projection in the albino rat. *Exp. Brain Res.* **49**, 410–418.
- Durbin, R., and Mitchison, G. (1990). A dimension reduction framework for understanding cortical maps. *Nature* **343**, 644–647.
- Felleman, D.J., and Van Essen, D.C. (1991). Distributed hierarchical processing in the primate cerebral cortex. *Cereb. Cortex* **1**, 1–47.
- Garrett, M.E., Nauhaus, I., Marshel, J.H., and Callaway, E.M. (2014). Topography and areal organization of mouse visual cortex. *J. Neurosci.* **34**, 12587–12600.
- Goodhill, G.J., and Willshaw, D.J. (1990). Application of the elastic net algorithm to the formation of ocular dominance stripes. *Netw. Comput. Neural Syst.* **1**, 41–59.
- Hasson, U., Levy, I., Behrmann, M., Hendler, T., and Malach, R. (2002). Eccentricity bias as an organizing principle for human high-order object areas. *Neuron* **34**, 479–490.
- Houzel, J.C., Carvalho, M.L., and Lent, R. (2002). Interhemispheric connections between primary visual areas: beyond the midline rule. *Braz. J. Med. Biol. Res.* **35**, 1441–1453.
- Hubel, D.H., and Livingstone, M.S. (1987). Segregation of form, color, and stereopsis in primate area 18. *J. Neurosci.* **7**, 3378–3415.
- Hubel, D.H., and Wiesel, T.N. (1967). Cortical and callosal connections concerned with the vertical meridian of visual fields in the cat. *J. Neurophysiol.* **30**, 1561–1573.
- Innocenti, G.M., Manger, P.R., Masiello, I., Colin, I., and Tettoni, L. (2002). Architecture and callosal connections of visual areas 17, 18, 19 and 21 in the ferret (*Mustela putorius*). *Cereb. Cortex* **12**, 411–422.
- Jbabdi, S., Sotiropoulos, S.N., and Behrens, T.E. (2013). The topographic connectome. *Curr. Opin. Neurobiol.* **23**, 207–215.
- Juavinett, A.L., Nauhaus, I., Garrett, M.E., Zhuang, J., and Callaway, E.M. (2017). Automated identification of mouse visual areas with intrinsic signal imaging. *Nat. Protoc.* **12**, 32–43.
- Kaas, J.H. (1997). Topographic maps are fundamental to sensory processing. *Brain Res. Bull.* **44**, 107–112.

- Kaas, J.H., Hall, W.C., Killackey, H., and Diamond, I.T. (1972). Visual cortex of the tree shrew (*Tupaia glis*): architectonic subdivisions and representations of the visual field. *Brain Res.* 42, 491–496.
- Kaas, J.H., Krubitzer, L.A., and Johanson, K.L. (1989). Cortical connections of areas 17 (V-I) and 18 (V-II) of squirrels. *J. Comp. Neurol.* 287, 426–446.
- Kamps, F.S., Hendrix, C.L., Brennan, P.A., and Dilks, D.D. (2020). Connectivity at the origins of domain specificity in the cortical face and place networks. *Proc. Natl. Acad. Sci. USA* 117, 6163–6169.
- Kaskan, P.M., Lu, H.D., Dillenburger, B.C., Kaas, J.H., and Roe, A.W. (2009). The organization of orientation-selective, luminance-change and binocular-preference domains in the second (V2) and third (V3) visual areas of New World owl monkeys as revealed by intrinsic signal optical imaging. *Cereb. Cortex* 19, 1394–1407.
- Lyon, D.C., Jain, N., and Kaas, J.H. (1998). Cortical connections of striate and extrastriate visual areas in tree shrews. *J. Comp. Neurol.* 401, 109–128.
- Majka, P., Chaplin, T.A., Yu, H.H., Tolpygo, A., Mitra, P.P., Wójcik, D.K., and Rosa, M.G.P. (2016). Towards a comprehensive atlas of cortical connections in a primate brain: Mapping tracer injection studies of the common marmoset into a reference digital template. *J. Comp. Neurol.* 524, 2161–2181.
- Manger, P.R., Kiper, D., Masiello, I., Murillo, L., Tettoni, L., Hunyadi, Z., and Innocenti, G.M. (2002). The representation of the visual field in three extrastriate areas of the ferret (*Mustela putorius*) and the relationship of retinotopy and field boundaries to callosal connectivity. *Cereb. Cortex* 12, 423–437.
- Marshel, J.H., Garrett, M.E., Nauhaus, I., and Callaway, E.M. (2011). Functional specialization of seven mouse visual cortical areas. *Neuron* 72, 1040–1054.
- Mathis, A., Mamidanna, P., Cury, K.M., Abe, T., Murthy, V.N., Mathis, M.W., and Bethge, M. (2018). DeepLabCut: markerless pose estimation of user-defined body parts with deep learning. *Nat. Neurosci.* 21, 1281–1289.
- Minciacchi, D., and Antonini, A. (1984). Binocularity in the visual cortex of the adult cat does not depend on the integrity of the corpus callosum. *Behav. Brain Res.* 13, 183–192.
- Mishkin, M., and Ungerleider, L.G. (1982). Contribution of striate inputs to the visuospatial functions of parieto-preoccipital cortex in monkeys. *Behav. Brain Res.* 6, 57–77.
- Mundinano, I.-C., Kwan, W.C., and Bourne, J.A. (2015). Mapping the mosaic sequence of primate visual cortical development. *Front. Neuroanat.* 9, 132.
- Najafian, S., Jin, J., and Alonso, J.M. (2019). Diversity of Ocular Dominance Patterns in Visual Cortex Originates from Variations in Local Cortical Retinotopy. *J. Neurosci.* 39, 9145–9163.
- Nath, T., Mathis, A., Chen, A.C., Patel, A., Bethge, M., and Mathis, M.W. (2019). Using DeepLabCut for 3D markerless pose estimation across species and behaviors. *Nat. Protoc.* 14, 2152–2176.
- Olivarria, J.F., and Abel, P.L. (1996). The distribution of callosal connections correlates with the pattern of cytochrome oxidase stripes in visual area V2 of macaque monkeys. *Cereb. Cortex* 6, 631–639.
- Pachitariu, M., Stringer, C., Dipoppa, M., Schröder, S., Rossi, L.F., Dalgleish, H., Carandini, M., and Harris, K.D. (2017). Suite2p: beyond 10,000 neurons with standard two-photon microscopy. *bioRxiv*. <https://doi.org/10.1101/061507>.
- Peirce, J., Gray, J.R., Simpson, S., MacAskill, M., Höchenberger, R., Sogo, H., Kastman, E., and Lindeløv, J.K. (2019). PsychoPy2: Experiments in behavior made easy. *Behav. Res. Methods* 51, 195–203.
- Roe, A.W., and Ts'o, D.Y. (1995). Visual topography in primate V2: multiple representation across functional stripes. *J. Neurosci.* 15, 3689–3715.
- Rosa, M.G.P. (1997). *Visuotopic Organization of Primate Extrastriate Cortex* (Boston, MA: Springer), pp. 127–203.
- Rosa, M.G.P. (2002). Visual maps in the adult primate cerebral cortex: some implications for brain development and evolution. *Braz. J. Med. Biol. Res.* 35, 1485–1498.
- Rosa, M.G.P., and Krubitzer, L.A. (1999). The evolution of visual cortex: where is V2? *Trends Neurosci.* 22, 242–248.
- Rosa, M.G.P., and Manger, P.R. (2005). Clarifying homologies in the mammalian cerebral cortex: the case of the third visual area (V3). *Clin. Exp. Pharmacol. Physiol.* 32, 327–339.
- Rosa, M.G.P., Sousa, A.P.B., and Gattass, R. (1988). Representation of the visual field in the second visual area in the Cebus monkey. *J. Comp. Neurol.* 275, 326–345.
- Rosa, M.G.P., Fritsches, K.A., and Elston, G.N. (1997). The second visual area in the marmoset monkey: visuotopic organization, magnification factors, architectonical boundaries, and modularity. *J. Comp. Neurol.* 387, 547–567.
- Sanides, D., and Albus, K. (1980). The distribution of interhemispheric projections in area 18 of the cat: coincidence with discontinuities of the representation of the visual field in the second visual area (V2). *Exp. Brain Res.* 38, 237–240.
- Schindelin, J., Arganda-Carreras, I., Frise, E., Kaynig, V., Longair, M., Pietzsch, T., Preibisch, S., Rueden, C., Saalfeld, S., Schmid, B., et al. (2012). Fiji: an open-source platform for biological-image analysis. *Nat. Methods* 9, 676–682.
- Schira, M.M., Wade, A.R., and Tyler, C.W. (2007). Two-dimensional mapping of the central and parafoveal visual field to human visual cortex. *J. Neurophysiol.* 97, 4284–4295.
- Schneider, G.E. (1969). Two visual systems. *Science* 163, 895–902.
- Schwartz, E.L. (1977). The development of specific visual connections in the monkey and the goldfish: outline of a geometric theory of receptotopic structure. *J. Theor. Biol.* 69, 655–683.
- Schwartz, E.L. (1983). Cortical mapping and perceptual invariance: a reply to Cavanagh. *Vision Res.* 23, 831–835.
- Sereno, M.I., McDonald, C.T., and Allman, J.M. (1994). Analysis of retinotopic maps in extrastriate cortex. *Cereb. Cortex* 4, 601–620.
- Sereno, M.I., McDonald, C.T., and Allman, J.M. (2015). Retinotopic organization of extrastriate cortex in the owl monkey—dorsal and lateral areas. *Vis. Neurosci.* 32, E021.
- Sesma, M.A., Casagrande, V.A., and Kaas, J.H. (1984). Cortical connections of area 17 in tree shrews. *J. Comp. Neurol.* 230, 337–351.
- Sheth, B.R., and Young, R. (2016). Two visual pathways in primates based on sampling of space: Exploitation and exploration of visual information. *Front. Integr. Neurosci.* 10.
- Shipp, S., and Zeki, S. (2002). The functional organization of area V2, II: the impact of stripes on visual topography. *Vis. Neurosci.* 19, 211–231.
- Sincich, L.C., Adams, D.L., and Horton, J.C. (2003). Complete flatmounting of the macaque cerebral cortex. *Vis. Neurosci.* 20, 663–686.
- Tootell, R.B.H., Silverman, M.S., De Valois, R.L., and Jacobs, G.H. (1983). Functional organization of the second cortical visual area in primates. *Science* 220, 737–739.
- Tusa, R.J., Rosenquist, A.C., and Palmer, L.A. (1979). Retinotopic organization of areas 18 and 19 in the cat. *J. Comp. Neurol.* 185, 657–678.
- Viswanathan, S., Williams, M.E., Bloss, E.B., Stasevich, T.J., Speer, C.M., Nern, A., Pfeiffer, B.D., Hooks, B.M., Li, W.P., English, B.P., et al. (2015). High-performance probes for light and electron microscopy. *Nat. Methods* 12, 568–576.
- Wang, Q., and Burkhalter, A. (2007). Area map of mouse visual cortex. *J. Comp. Neurol.* 502, 339–357.
- Wolf, F., Bauer, H.U., and Geisel, T. (1994). Formation of field discontinuities and islands in visual cortical maps. *Biol. Cybern.* 70, 525–531.
- Wong, P., and Kaas, J.H. (2009). Architectonic subdivisions of neocortex in the tree shrew (*Tupaia belangeri*). *Anat. Rec.* 292, 213–223.
- Yu, H.H., Chaplin, T.A., and Rosa, M.G.P. (2015). Representation of central and peripheral vision in the primate cerebral cortex: Insights from studies of the marmoset brain. *Neurosci. Res.* 93, 47–61.
- Yu, H.-H., Rowley, D.P., Price, N.S.C., Rosa, M.G.P., and Zavitz, E. (2020). A twisted visual field map in the primate dorsomedial cortex predicted by topographic continuity. *Sci. Adv.* 6, eaaz8763.
- Zhuang, J., Ng, L., Williams, D., Valley, M., Li, Y., Garrett, M., and Waters, J. (2017). An extended retinotopic map of mouse cortex. *eLife* 6, 1–29.

STAR★METHODS

KEY RESOURCES TABLE

REAGENT or RESOURCE	SOURCE	IDENTIFIER
Antibodies		
Rat anti DYKDDDDK Tag	Aligent Technologies	200474; RRID:AB_10597743
Chicken anti GFP	Aves Lab, Inc	GFP1020; RRID: AB_10000240
Mouse anti dsRed	Clontech	632392; RRID:AB_2801258
Rabbit anti myc	Abcam	AB9106; RRID:AB_307014
Alexa 488 goat anti chicken	Molecular Probes	A11039; RRID:AB_142924
Alexa 568 goat anti mouse	Molecular Probes	A11103; RRID:AB_144696
CF405M goat anti rabbit	Biotium	20181; RRID:AB_10561325
CF647 goat anti rat	Biotium	20283; RRID:AB_10853786
Bacterial and virus strains		
AAV9-Syn.GCaMP6s.WPRE.SV40	Chen et al., 2013	Addgene 100843
AAV1.Syn.GCaMP6s.WPRE.SV40	Chen et al., 2013	Addgene 100843-AAV1
AAV1.CAG.tdtomato.WPRE.SV40	Gift from James Wilson	Addgene 105554
AAV1.CAG.Ruby2sm-Flag.WPRE.SV40	Vigene Biosciences	N/A
AAV1.CAG.GFPsm-myc.WPRE.SV40	Viswanathan et al., 2015	Addgene 98926
AAV1-hSYn1-axon-GCaMP6s	Vigene Biosciences	N/A
Experimental models: Organisms/strains		
Tree shrews	Max Planck Florida Institute for Neuroscience	N/A
Software and algorithms		
ScanImage v2019	Vidrio Technologies	http://scanimage.vidriotechnologies.com/display/SH;jsessionid=FACC3AA6BD554A5A634EC1F575E26880
MATLAB 2018	Mathworks	https://www.mathworks.com/products/matlab.html
Python 2.7, 3.6	Python Software Foundation	https://www.python.org/
Psychopy	Peirce et al., 2019	https://www.psychopy.org/
Suite2p	Pachitariu et al., 2017	https://github.com/MouseLand/suite2p
DeepLabCut	Mathis et al., 2018	https://github.com/DeepLabCut/DeepLabCut
ImageJ	Schindelin et al., 2012	https://imagej.net/software/fiji
SineFit (Sine fitting algorithm)	Peter Seibold	https://www.mathworks.com/matlabcentral/fileexchange/66793-sine-fitting
Simulation of retinotopic map formation	Madineh Sedigh-Sarvestani, modified from Yu et al. (2020)	https://zenodo.org/record/5522899

RESOURCE AVAILABILITY

Lead contact

Further information and requests for resources and reagents should be directed to and will be fulfilled by the lead contact, Madineh Sedigh-Sarvestani (msarvestani@gmail.com)

Materials availability

This study did not generate new unique reagents.

Data and code availability

- Due to the large size of the imaging dataset, the raw data have not been deposited in a public repository but will be made available upon request.

- Code for the mathematical simulation of retinotopic map formation can be found at <https://zenodo.org/record/5522899>. Other processing and analysis routines were written in MATLAB or Python and can be shared upon request.
- Any additional information required to reanalyze the data reported in this work paper is available from the Lead Contact upon request.

EXPERIMENTAL MODEL AND SUBJECT DETAILS

All experimental procedures were approved by the Max Planck Florida Institute for Neuroscience Animal Care and Use Committee and performed in compliance with guidelines published by the National Institutes of Health. Tree shrews (*Tupaia belangeri*) used in this study ($n = 15$) were either male or female, 8 months–2 years old and weighing 140–210 g. Animals were housed in single occupancy cages in a 12 hour lights on/off animal suite. Their food and water aliquots were given once daily but both were enough to maintain their weight and not considered as ‘restricted’.

METHOD DETAILS

Behavioral acclimation

Tree shrews were used for chronic recordings while awake or anesthetized for tracer injections followed by histology. Animals intended for chronic recording went through a 1–3 week period of behavioral acclimation to the awake recording setup. Some animals were water restricted during this period to help acclimation, although even the minimum daily water amount (10–15 ml) was enough to maintain their baseline weight. Following this period, a sterile surgery was performed to inject genetically encoded calcium indicators into the visual cortex. Following an expression period of 2–4 weeks, awake animals were imaged during several experiments, each lasting 0.5 to 1.5 hours. In rare cases when imaging sessions occurred after several weeks ‘off’, animals were given low doses (0.2x dose below) of a sedative (Midazolam) to reduce stress during imaging sessions.

Craniotomy and intra-cortical expression of viral vectors

Tree shrews were sedated with Midazolam (5 mg/kg, intramuscular (IM)), anesthetized with ketamine (75 mg/kg, IM) and given atropine (0.5 mg/kg, subcutaneous (SC)) to reduce secretions. A long-acting analgesic (slow-release Buprenorphine, 0.6 mg/kg, SC), as well as dexamethasone (1 mg/kg, IM) to reduce swelling, was administered before the surgery. The animal’s head was shaved, cleaned, and the surgical site was injected with a mixture of bupivacaine and lidocaine (0.3–0.5 ml, SC) to reduce local pain. Isoflurane anesthesia (0.5%–2.5%) was initially delivered through a nose-cone, and once the animal was stably anesthetized, via an endotracheal tube. A mechanical ventilator provided respiration at 100 strokes per minute. The animal’s EKG was monitored through leads placed on the chest and back. Venous cannulation (hind limb) was performed to deliver 5% dextrose solution. Internal temperature (36–37°C) was maintained by a thermostatically controlled heating pad while expired CO₂ and heart rate were monitored to assess anesthetic depth and overall health. The animal was placed in a stereotaxic device (Kopf, Model 900), a small incision was made over the midline, skin and muscle were retracted. A metal headplate was cemented (Metabond) to the anterior skull over the olfactory bulbs and a metal chamber (inner diameter 8 mm) was cemented to the skull over the visual cortex. A craniotomy was made within this chamber (about 6-mm diameter), centered at 4 mm anterior, 4 mm lateral relative to lambda, using a motorized jeweler’s drill. The visual cortex was injected with a total of 2–3 μ L of virus solution (1e13 GC/ml) containing AAV9-Syn-GCaMP6s.WPRE.SV40 (Penn Vector Core or Addgene) through a beveled glass micropipette (tip size 10–20 μ m diameter) using a nanoinjector (Drummond Nanoject II, WPI).

A total of 6–10 injection sites were made in each cranial window, while the dura remained intact. Pipettes with 10–30 μ m tips can penetrate the dura in adult tree shrews so long as the tip is beveled to a sharp point, precluding the need for a local durotomy. To facilitate spreading, the virus was delivered at two depths, 250 and 500 μ m below the cortical surface. After the injections, a durotomy was performed, and a 3–5 mm glass window, glued to an 8 mm coverglass was placed inside the craniotomy and sealed with Vet-bond. The surface of the metal chamber was covered with black dental cement to prevent light reflection. The skin around the incision was sutured closed. The animals were then placed on a heating blanket in a small cage to recover from anesthesia. The first imaging experiments occurred following a period of 2–3 weeks. The animals continued their acclimation to the recording apparatus during this time. Animals were given twice daily doses of Baytril (5 mg/kg) for 5 days to reduce the probability of infections.

Chronic recording setup and head fixation

All data, except that in [Figure S3E](#) was recorded in awake animals passively viewing visual stimuli on a monitor placed parallel to the eyes. The data in [Figure S3E](#) was recorded in isoflurane (1%) anesthetized animals. Animals were head-fixed to a home-built stereotax using metal screws that interfaced with the metal head-plate previously cemented to the skull. The stereotax also included a clear acrylic tube that served to constrain the animal’s body movements. Animals were acclimated to this setup prior to and after the injection surgery using juice rewards. During imaging experiments, some animals were rewarded with juice after the completion of stimulus blocks, but no animals received juice within stimulus experiments.

Eye tracking

Because we measured retinotopic maps in awake animals, we needed to rule out the influence of eye movements on functional maps. We therefore recorded eye movements in awake head-fixed tree shrews during the presentation of moving bar retinotopic stimuli. We used an infrared camera (FLIR Systems Grasshopper3) with a macro lens, coupled with an infrared LED light source to record the contralateral (right eye, imaging window in left hemisphere) at 60 Hz. The imaging plane was approximately parallel to the contralateral eye. We cropped the resulting video to include just the eye and used the open-source model-based tracking software DeepLabCut (Mathis et al., 2018; Nath et al., 2019) to track the pupil along 8 points (Figure S1D; Video S4). We manually placed markers on 20–40 frames for training the model and visually verified that the pupil was correctly tracked on every frame. The 8 tracking points were then fit to an ellipse using a simple script. The center of the ellipse served as the center position of the pupil and the major axis of the ellipse served as the pupil diameter.

To convert changes in pupil position in units of mm ($position_x$) from the recorded video to units of visual degrees ($angular_position_x$) reflecting angular position we used an eyeball radius (r) of 3.9 mm for adult tree shrews (Bobier et al., 1992). The center of the pupil ($center_x$) on the first video frame of the recording was used as a reference point for the eye position.

$$angular_position_x = \arcsin\left(\frac{position_x - center_x}{r}\right) \quad (1)$$

$$angular_position_y = \arcsin\left(-\frac{position_y - center_y}{r}\right) \quad (2)$$

We further confirmed the accuracy of this unit conversion by measuring the displacement in mm resulting from angular rotation of a spherical ball 7.8 mm in diameter. The ball was placed on a manual rotating stage and placed in approximately the same position as the tree shrew eye would be during recording sessions.

Calcium imaging experiments

Wide-field 1-photon and two-photon calcium imaging was performed using the Bergamo II Scope (Thorlabs) with blue LED illumination using an LED driver (Thorlabs). GCaMP6s fluorescence signal from the cortical surface was acquired at about 15 Hz (640×540 pixels, field of view (FOV) ranges from 3×3 to 5×5 mm²) using a Zyla 5.5 sCMOS camera (Andor) controlled by μ Manager2. Average excitation power at the exit of the air objective (2x or 4x, UPlanFI, Olympus) ranged from 0.2 to 0.8 mW. Individual sessions were initially registered prior to recording using a blood vessel template recorded on the first chronic session. More accurate registration was performed offline using custom scripts based on pixel correlation. Single-condition response maps were expressed as $\frac{\Delta F}{F} = \frac{F_{stim} - F_o}{F_o}$ where F_{stim} is the trial and time-averaged response across stimulus frames, and F_o is the trial and time-averaged response during the 1 s prior to stimulus onset.

Two-photon imaging experiments

Imaging experiments were performed using the Bergamo II Scope (Thorlabs) with either 920 nm excitation provided by an InSight Dual (Spectra-Physics) or 920 nm excitation provided by a Mai Tai DeepSea laser (Spectra-Physics), controlled by ScanImage software (Vidrio Technologies). Average excitation power at the exit of the objective (16x, CFI75, Nikon Instruments) ranged from 20 to 50 mW. Images were acquired at 15 Hz (512×512 pixels, field of view (FOV) ranges from 0.44×0.44 mm² to 1.1×1.1 mm²). Imaging depth was between 75 and 200 μ m below the surface, corresponding to Layer 2/3 of the tree shrew visual cortex. Z-projections of two-photon fields of view were aligned to the epi-fluorescence imaging with the blood vessel pattern. Registration and Single-cell ROIs selection was done automatically using Suite2P (Pachitariu et al., 2017). The response to each stimulus was calculated as $\frac{\Delta F}{F} = \frac{F_{stim} - F_o}{F_o}$ where F_{stim} is the response during each frame when the stimulus was on, and F_o is the time-averaged response during the 1 s prior to stimulus onset. Except where noted, visual stimuli for 2-photon experiments were presented for 3 s, with a 3 s inter-stimulus interval.

Visual stimulus methods

Visual stimuli were delivered on a monitor using PsychoPy (Peirce et al., 2019). The monitor had resolution 1920×1080 pixels and at the typical distance of 20 cm from the eyes extended $\sim 120 \times 70^\circ$. The center of the monitor, defined as (0,0) was matched to the mid-point between the two eyes. As described above, the animals were stationary and head-fixed during passive viewing of all visual stimuli, except the coarse receptive field mapping stimuli in Figure S3E. The eyes were on a horizontal plane (the microscope rotated to achieve parallel plane). The monitor was placed parallel to the eyes at a distance of 20 cm.

Retinotopic mapping stimuli consisted of moving black bars on a gray screen, with a width of 3° , which moved at 4° per second either horizontally for phase-encoded azimuth mapping or vertically for phase-encoded elevation mapping. Between 30–50 trials were used for each condition. For each new animal, the first stage of retinotopy mapping included showing full-screen stimuli to discover the limited range of the visual field that activated neurons in portions of V1 and V2 within the cranial window. This was done with the monitor parallel to the animal (Figure S1A) at a distance of 20 cm, covering 116° of azimuth and with the monitor placed

at 45° relative to midline, approximately parallel to the contralateral eye at a distance of 13 cm, to cover up to 130° of azimuth space. For monitors placed close (13 cm) to the eye, spherically corrected stimuli were used (Marshall et al., 2011; Zhuang et al., 2017). Following this procedure, stimuli were then shown in the relevant limited portion of the visual field. For the animal in Figure S5F, polar stimuli were used to measure retinotopic maps in polar coordinates. We used Cartesian maps previously measured in the same animal to determine the location on the monitor corresponding to 0 azimuth and 0 elevation and centered the polar stimuli on this point. Black rings 5° in thickness expanded from 0 to 25° in 8 s, on a gray background. Black wedges, 15° in thickness rotated clockwise 360° starting with the 90° position, in 8 s. 30 trials were repeated for each condition.

To determine the relative sensitivity to monocular or binocular visual stimuli, moving edge stimuli were shown in the binocular condition, with both eyes un-occluded, and in the monocular condition, with the eye ipsilateral to the imaging window occluded (Kaskan et al., 2009). The moving edge covered the relevant portion of the visual field, typically 25° of ipsilateral and contralateral. Only vertical moving edges were used and 30–50 trials were run. Binocular sensitivity maps produced using drifting gratings produced qualitatively similar results. All other stimuli were shown in the binocular condition.

To evoke responses related to horizontal disparity, correlated red/green random dot stereograms were used in conjunction with red/green filtered goggles placed on the animal's eyes. The combination of the red/green filters and the relative position of the red and green dots on the monitor produced stereograms with uncrossed and crossed disparities in a range between +1.5 and –1.5°. Dots drifted in 1 of 8 different directions, and had a range of inter-ocular horizontal disparities encoded by a range of different horizontal distances between the center of red and green dots. At zero disparity, the red/green dots merged into a single yellow drifting dot. The stimulus covered ± 30° of azimuth and elevation. The remaining background space of the monitor was filled with static yellow dots with the same density as the moving dots within the visual field. 10 trials were run for disparity measurements at the wide-field and two-photon level. For wide-field maps exhibiting disparity sensitivity, each trial consisted of 8 directions of drifting dot motion and two disparities (0, –1.5). For two-photon measurements, the goal was to quantify the disparity tuning curve, therefore each trial consisted of a single direction, corresponding to the preferred direction of motion in the field of view, and 13 disparities. Stimulus duration was 2 s, with a 2 s inter stimulus interval.

To map receptive fields, the relevant portion of the visual field corresponding to the two-photon field of view was identified using small apertures with drifting gratings at all orientations. A 20x20° box was centered over this region, and split into 2x2° squares. Each square was randomly flashed for 0.5 s, followed by a 1 s inter-stimulus-interval. 20 –30 trials were repeated.

Tracer injections

Some animals were injected with AAV viral tracers in V1, in order to map out the rules of connectivity between V1 and V2. Animals in which we recorded functional calcium data were also processed for histology. In addition to AAV9-Syn-GCaMP6s.WPRE.SV40 used for tree shrew functional maps, we used the following viral constructs.

- Figure 4B: AAV1.CAG.tdtomato.WPRE.SV40
- Figure 4C (left): AAV1.CAG.Ruby2sm-Flag.WPRE.SV40, AAV1.CAG.GFPsm-myc.WPRE.SV40, AAV9-Syn-GCaMP6s.WPRE.SV40
- Figure 4C (right): AAV1-hSYn1-axon-GCaMP6s, AAV1.CAG.tdtomato.WPRE.SV40
- Figure 4D: AAV1.CAG.GFPsm-myc.WPRE.SV40, AAV1.CAG.tdtomato.WPRE.SV40
- Figure 4E: AAV1.CAG.tdtomato.WPRE.SV40
- Figure 5A: AAV1.CAG.GFPsm-myc.WPRE.SV40
- Figure 5B: Same as Figure 4C (right)
- Figure 5C: AAV1.CAG.tdtomato.WPRE.SV40
- Figure S4A (leftmost): AAV1.CAG.GFPsm-myc.WPRE.SV40
- Figure S4A (middle two): AAV1.CAG.GFPsm-myc.WPRE.SV40
- Figure S4A (rightmost): AAV1.CAG.tdtomato.WPRE.SV40
- Figure S4B (left two): AAV1.CAG.Ruby2sm-Flag.WPRE.SV40, AAV1.CAG.GFPsm-myc.WPRE.SV40, AAV9-Syn-GCaMP6s.WPRE.SV40
- Figure S4B (right): Same as Figure 4C (right)
- Figure S4E: Same as Figure 4E

The GCaMP6s virus was used for green fluorescent tracer labeling, the tdtomato for red, and the two spaghetti monster (Jbabdi et al., 2013) variants were paired with secondary fluorophores in either blue or far-red. This allowed us to get up to 4 color labeling in one animal. Viral tracers were injected intracranially as described in the surgical procedures above. Perfusion and histology was done following a 3–4 week expression period. We show anatomical data from $n = 11$ separate tree shrews in the main and supporting figures. Our conclusions were based on additional data from a separate $n = 9$ separate tree shrews. For mapping the retinotopic pattern of connections from V1 to V2 (of the same hemisphere), we base our conclusions on the 8 animals shown in Figures 4 and S4 as well as an additional 5 animals. For understanding the relationship between V1 terminal projections and the functional retinotopy map, we used data from 2 animals in addition to the 1 shown in Figure 4E. For understanding the pattern of callosal terminal zones in V2, we used data from the 3 animals shown in Figure 5 plus an additional 2 animals.

Fixation and immunostaining

Animals received a lethal injection of the barbiturate Euthasol and were perfused transcardially with 0.9% NaCl in 0.1 M PB, followed by 2 or 4% paraformaldehyde (PFA). Once the brain was extracted, the two hemispheres were separated and each cortical hemisphere was flattened in PFA between two glass slides with a weight on top. Hemispheres were then transferred to a 30% sucrose in 0.1M PB solution and stored 4°C until sectioning. A freezing sliding microtome (Leica SM2010 R) was used to cut 50- μ m-thick sections parallel to the flattened surface. Slices were rinsed once in PB, washed three times in phosphate buffered saline (PBS) followed by an incubation of one hour in blocking buffer (2% normal goat serum, Jackson ImmunoResearch, Cat # 017-000-121, 0.3M NaCl, 1% Bovine Serum Albumin, Sigma, Cat#A2153, 0.3% Triton X-100, in 0.1M PB). Slices were then incubated for 10–12 hr in blocking buffer containing primary antibodies (Rat anti DYKDDDDK Tag at 1:500, Aligent Technologies 200474; Chicken anti GFP at 1:1000, Aves Lab, Inc GFP1020; Mouse anti dsRed at 1:1000, Clontech 632392; Rabbit anti myc at 1:500, Abcam AB9106). After washing three times in PBS, slices were incubated for 2 hr in blocking buffer containing 1:500 (Alexa 488 goat anti chicken Molecular Probes, ab1500169; Alexa 568 goat anti mouse, Molecular Probes A11031; CF405M goat anti rabbit, Biotium 20373; and CF647 goat anti rat, Biotium 20283). Slices were washed two times using 1X PBS, then washed once more in 0.1M PB then mounted to a slide using SlowFade Gold (ThermoFisher Scientific) and imaged using a fluorescence microscope (Olympus BX53). Image processing was done using ImageJ (Schindelin et al., 2012).

Alignment of functional maps with anatomical data from the same animal

In Figure 5C, we provide a histological section showing callosal projections in V1 and V2 originating from injections in contralateral V1. We show the portion of the sectioned brain tissue matching our imaging window. To obtain this section, we match the blood vessel pattern on the histology section to the blood vessel pattern in our imaging window captured *in vivo* using the wide-field camera. We use the circular indent produced by the window on the brain as well as the outline of major blood vessels as matching anchors. Using these two anchors we manually shifted a 50% transparent duplicate of the histology image (while preserving original aspect ratio) until satisfactory alignment of major blood vessels and window outline was achieved between the histology image and the blood-vessel image within our imaging window.

Data Analysis

Analysis was performed using custom scripts in MATLAB or Python.

Azimuth and elevation, produced by moving bar stimuli (Figure 1A), were phase-encoded, where the temporal phase of the horizontal or vertical drifting bar directly encodes iso-azimuth and iso-elevation coordinates on the stimulus monitor. Therefore estimating the temporal delay of the response for each cortical pixel can be used to localize the region of the visual field to which the pixel neurons respond best. For each cortical pixel, the phase of the first harmonic at the stimulus frequency (1/period) was determined using a discrete Fourier transform of the trial-averaged time-series for each motion condition. 30–50 trials were run for each condition. The stimulus-response delay due to the rise-time of the calcium indicator was calculated by subtracting phase maps produced by bars moving in opposite directions. Delay-corrected maps were produced by subtracting this delay. Finally, maps were smoothed with a zero-phase digital ‘hamming’ filter with window width of 100 μ m.

For retinotopy maps, an iterative algorithm was used to produce blood-vessel free maps (compare Azimuth map in Figures 1D and 5C). A highpass Gaussian spatial filter was used to detect the outline of blood vessels, producing a blood vessel outline. The mask was then filled to produce a blood vessel mask. Pixels within the blood vessel mask were removed from retinotopy map images and replaced with an average of their nearest neighbors, produced with a hamming filter of size 200 μ m.

The medial and lateral border of V2 were determined based on the retinotopic maps. As shown previously, the lateral portion of V1 consists a compressed representation of up to 30° of the ipsilateral visual field, the lateral edge of which aligns well with the cytoarchitecturally defined border of V1 (Bosking et al., 2000). We used the lateral edge of this region to designate the V1/V2 border (Figure S1B, top). In animals where we had combined functional maps and anatomical tracer data, this border coincided well with the lateral edge of callosal terminals (Figure 5C) and the medial edge of terminals produced by injections in ipsilateral V1 (Figures 4E and 4F). For demarcating the lateral border of V2, we used the midpoint of discontinuity in the elevation map (red blob in Figure S1B, bottom). This discontinuous representation of the lower visual field is related to the border of a nearby visual area TD (Wong and Kaas, 2009). Further studies are needed to gain insight into the retinotopic maps of visual areas beyond V2. This demarcation was consistent with the known width of V2 based on previous cytoarchitecture studies (Wong and Kaas, 2009) and our own tracer injection studies.

Linear cortical magnification factor (CMF) maps (Figure S2) were calculated as the inverse of the gradient of the smoothed (500 μ m nearest neighbor filter) azimuth or elevation maps. Gradient maps were calculated using the central difference where the gradient of a pixel is a weighted difference of its immediately neighboring pixels. CMF maps were thresholded to the central 99% percentile to remove outlier pixels with extreme values.

Maps of relative binocularity (Figure 5) were calculated from subtracting the magnitude map of responses during binocular viewing of retinotopic mapping stimuli from the magnitude map of responses measured during monocular viewing of the same stimuli (Kaskan et al., 2009). Monocular viewing refers to viewing condition with physically blocked ipsilateral eye (left eye when imaging window is in the left hemisphere) so that all visual input is seen through the contralateral eye only. The resulting map was thresholded between ± 1 SD of the mean and normalized to allow quantitative comparison with other maps.

Disparity analysis was carried out at both single-cell and wide-field scales since there has been little prior work on disparity sensitivity in the tree shrew visual system. For two-photon single-cell recordings, random dot stereograms drifted at the preferred direction of the FOV. Each trial consisted of 11–13 inter-ocular horizontal disparities ranging from -1.5 to 1.5° . This allowed us to produce single-cell disparity tuning curves (Figures S5A and S5B). The preferred disparity for each neuron (Figure S5B) was determined based on the horizontal disparity which produced the maximum average response across trials. For wide-field recordings covering regions with many different direction preferences, stereograms were shown with 8 drifting directions and only two horizontal disparities (-1.5 and 0). The single-condition maps for each direction and horizontal disparity were calculated using the $\frac{\Delta F}{F}$ as described above. Then the single-condition maps were vector-summed (without angle doubling) for all 8 orientations to produce a single-condition-disparity map at -1.5° and another at 0° . To produce the disparity sensitivity map (Figure 5), the 0° map was subtracted from the -1.5° map.

Model methods

We used the elastic net algorithm (Goodhill and Willshaw, 1990; Yu et al., 2020), implemented as in Yu et al. (2020) and modified it for the formation of visual field maps in V2. We refer to Yu et al. (2020) and our published interactive code for the implementation of this algorithm (<https://zenodo.org/record/5522899>), and briefly describe the framework here.

V2 is modeled as a rectangular sheet, with variable aspect ratio, but fixed area consisting of 600 pixels or ‘neurons’. Each neuron has a point RF in the visual field, defined by its azimuth and elevation values. The neurons are initially arranged randomly on the visual field and cortex. The objective of the iterative algorithm is to arrange the neurons, using gradient descent, to minimize the cost function.

$$\text{Cost} = -k \sum_i \log \sum_j \Phi(x_i, y_j, k) + \beta_1 \sum_j \sum_{j' \in N(j)} \|y_j - y_{j'}\|^2 + \beta_2 \sum_{j \in B} \sum_{j' \in N_{V1}(j)} \|z_j - y_{j'}\|^2 + \beta_3 \left| \sum_j \sum_{j' \in N_{D1}(j)} \|y_j - y_{j'}\|^2 - \sum_j \sum_{j' \in N_{D2}(j)} \|y_j - y_{j'}\|^2 \right|$$

$$\Phi(x_i, y_j, k) = \exp\left(\frac{-\|x_i - y_j\|^2}{2k^2}\right), \text{ k is an annealing factor that reduces on each iteration.}$$

In simple terms, the target RF positions (x_i) are provided (Figure 3A, ‘Target VF’). At each iteration, the cost function produces a trade-off in minimizing the Euclidian distance between the RFs (y_j) and the target set of RFs (x_i) with several constraints applied to the relative position of neurons on the cortical surface. The first term is the main cost which is minimized when y_j is close to x_i , assuring optimal visual field coverage as in the ‘Target VF’. The second term, weighed by β_1 is minimized when RFs, and their nearby neighbors N on the cortex, are similar, ensuring smooth cortical maps. The third term, weighed by β_2 , is minimized when neurons at the border of the cortical area N_{V1} have RFs close to the vertical meridian. The border that V2 shares with V1 maps the vertical meridian in tree shrews and many other species. The fourth term, weighed by β_3 , is minimized when the RFs have nearby (± 3 pixels) neighbors that are similarly close along the two orthogonal directions of the cortical sheet. This ensures that the population receptive field for a group of nearby neurons on the cortical surface is not significantly stretched.

Parameters used: $k = 100$ and reduces by 0.05% on each iteration. The weights on the constraints c1, c2, c3 are $\beta_1 = \beta_2 = \beta_3 = 0.03$, except for simulations in Figures 3B and 3C and associated Figures S3A and S3B where $\beta_1 = 0.03$ $\beta_2 = \beta_3 = 0$ and thus the only acting constraint was c1, and simulations in Figure S3F where $\beta_1 = \beta_2 = 0.03$ and $\beta_3 = 0$, with only the first two constraints. We note that not although a wide range of parameter values reproduce our results, not all parameter choices produce qualitatively similar results as those shown in Figure 3. We chose parameters that produced smooth orthogonal maps at low aspect ratios, and observed changes in cortical maps that occurred as a function of increasing the aspect ratio.

QUANTIFICATION AND STATISTICAL ANALYSIS

All analyses and statistical tests were performed in MATLAB. Reported statistics represent population data across $n = 6$ animals, unless otherwise noted. Population means are mean \pm SD. Statistical test results are found in figure legends, and when relevant, duplicated in Results. When comparing differences in paired conditions (Figure 2C; Figure S2), the two-sample Wilcoxon rank sum test was used. For fitting the retinotopy gradients to sine functions in Figure 2, the publicly available sineFit package for MATLAB was used (Key resources table). Pixel-wise correlations between different map types in Figure 5 were reported as mean \pm SE, and were calculated based on a mask manually drawn around the extent of V2 in the imaging window, using MATLAB’s built-in ‘roipoly’ function. Pixel-wise correlations were calculated for each pair of maps (e.g., retinotopy versus relative binocularity) using Pearson’s r . The standard error around the mean for each r value was calculated using the bootstrap method, with 1000 bootstraps drawn randomly with replacement. The standard deviation of the Pearson r bootstrapped sampling distribution was reported as the SE of the mean correlation value for each map pairing. Visual inspection of data distributions were used to determine if the data met assumptions of the statistical approach. No statistical tests were used to predetermine sample size.